Contrib Mineral Petrol (1993) 113:1–8

Contributions to Mineralogy and Petrology

Experimental cpx/melt partitioning of 24 trace elements

Stanley R. Hart[1] **and Todd Dunn**[2]

[1] Department of Geology and Geophysics, Woods Hole Oceanographic Institution, Woods Hole, MA 02540 USA
[2] Department of Geology, University of New Brunswick, Fredericton, N.B., Canada E3B 5A3

Received June 18, 1992 / Accepted September 21, 1992

Abstract. Cpx/melt partition coefficients have been determined by ion probe for 24 trace elements at natural levels in an alkali basalt experimentally equilibrated at 1,380° C and 3 GPa. One goal was to intercompare Ds for both high-field-strength elements and rare earth elements (REE) in a single experiment. Relative to the REE spidergram, Hf and Ti show virtually no anomaly, whereas Zr exhibits a major negative anomaly. Other incompatible elements (Ba, K, Nb) fall in the range of published values, as do elements such as Sr, Y, Sc, Cr and V. Pb shows a value intermediate between La and Ce. Values for Be, Li and Ga are reported for the first time, and show that Be is as incompatible as the light REEs whereas Li and Ga are somewhat more compatible than the heavy REE.

Introduction

Clinopyroxene (Cpx) plays a key role in the partitioning of many trace elements during mantle melting and magmatic differentiation processes. The classic early papers of Schnetzler and Philpotts (1968), Onuma et al. (1968) and Nagasawa and Wakita (1968) utilized natural Cpx phenocryst/matrix pairs to determine trace element partition coefficients (Ds). This work was soon followed by the first attempts to determine partition coefficients on experimental Cpx/melt pairs (Masuda and Kushiro 1970; Green et al. 1971; Seward 1971). Subsequently, a large literature has evolved on the subject; the range of partition coefficients reported for individual elements is quite large, typically a factor of 2–10. Despite many efforts to understand the parameters responsible for this range (e.g., Lindstrom and Weill 1978; Dunn and McCallum 1982; Ray et al. 1983; Nielsen 1985), there is as yet no satisfactory model. Rarely do any of the published works treat more than a limited number of elements, thus it is not generally possible to combine data sets from different studies to create an internally consistent set of partition coefficients. This problem is particularly acute, for example, in studies (Salters and Hart 1989; Kelemen et al. 1990) which attempt to model both rare earth and high-field-strength elements (REE, HFSE), as there is no single study which reports experimental partition coefficients for both these groups of elements.

The present study provides ion probe Cpx/melt partitioning data for 24 trace elements, for a single experiment run at 1,380° C and 3 Gpa on a natural basalt composition with natural trace element concentrations. Wo do not address the issue of the P, T or X dependence of various trace element Ds; we attempt only to consistently relate a large group of Ds to each other as precisely as possible, at a P–T condition relevant to deep partial melting.

Correspondence to: S.R. Hart

Experimental details

The starting material was a chip of glass made by fusing a natural alkali olivine basalt (MB-41) from British Columbia. This sample was powdered, dried at 110° C, packed into a spectroscopic grade graphite capsule and fired briefly to red heat. This capsule was in turn enclosed in AlSiMag, graphite heater, Pyrex sleeve and talc sleeve, and run in a 1/2 inch piston cylinder press at 3 GPA and 1,380° C. The sample was taken directly to run temperature, held for 22 hours, and quenched. Run temperature was monitored with a $Pt-Pt_{87}Rh_{13}$ thermocouple located within 0.5 mm of the top of the capsule. No pressure correction was applied to the thermocouple EMF and temperatures are thought to be accurate to within $\pm 10°$ C. Pressure was monitored with a bourdon tube gauge. The reported pressure is thought to be accurate to within ± 0.1 GPa based on measurement of the melting point of NaCl by DTA. The run product was composed of clear brown glass, 0.064 cm^2 in cross-sectional area, with two contiguous clinopyroxene crystals of 0.0072 cm^2 cross-sectional area lodged in one corner of the capsule (Fig. 1a); the Cpx thus represents ~10% crystallization of the charge. Each crystal is optically uniform, though there is a small (15°) difference in extinction orientation between the two crystals.

The major element compositions of the two phases are given in Table 1, determined with a JEOL 6400 scanning electron microscope equipped with a Link eXL energy dispersive analyzer and

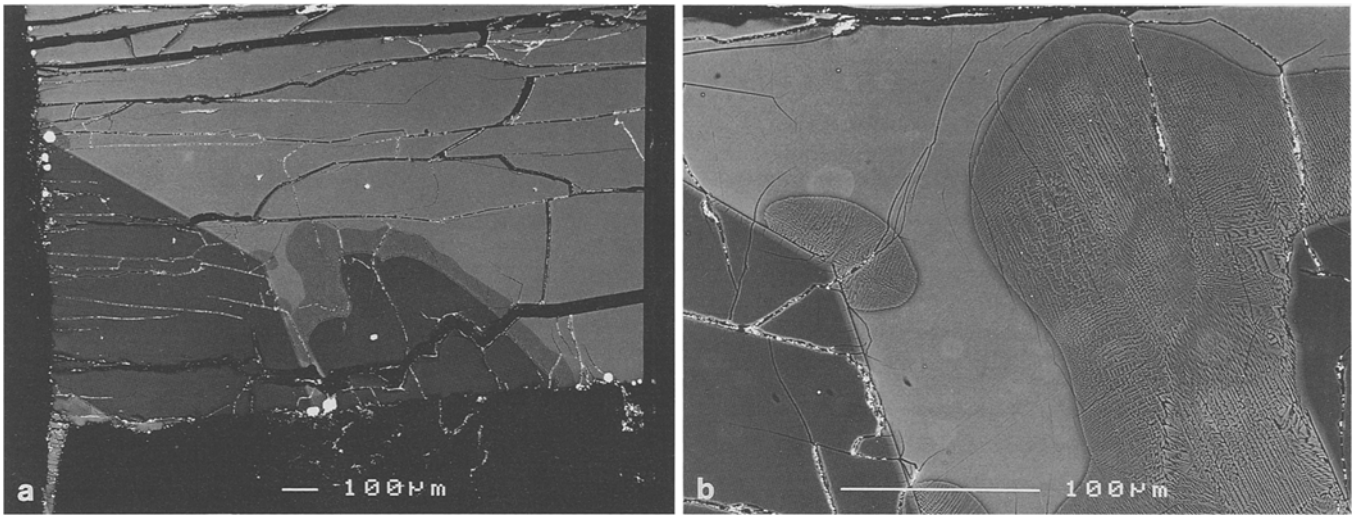

Fig. 1a, b. Electron backscatter images of the crystalline portion of the experimental charge: **a** low magnification image showing the two pyroxene crystals, dark gray, and surrounding glass, light gray. Note the zone of apparent quench crystallization surrounding the smaller crystal. **b** Higher magnification image of spinifex textured quench crystallized zone between the two crystals

Table 1. Electron microprobe analysis of bulk glass, spinifex textured quench zones and Cpx, sample MB-41

Oxide	Glass $n=9$	Spinifex quench material				Low-Ti Cpx $n=25$	High-Ti Cpx $n=10$
		24×24	12×12	6×6	Point		
SiO_2	47.67 (51)	47.85	47.80	47.69	48.91	49.17	49.11
TiO_2	2.61 (12)	2.66	2.55	2.65	2.51	0.98	1.55
Al_2O_3	16.06 (40)	16.07	16.02	16.29	16.39	14.14	13.93
MgO	5.91 (23)	5.76	5.75	5.80	5.61	10.50	10.79
CaO	9.50 (20)	9.45	9.59	9.32	9.21	15.24	16.57
MnO	0.23 (09)	0.17	0.23	0.17	n.d.	0.08	0.09
FeO[a]	10.88 (17)	11.00	10.98	10.78	11.08	6.61	5.61
Na_2O	3.92 (17)	3.97	4.00	3.75	3.62	2.94	2.64
K_2O	1.34 (11)	1.40	1.30	1.44	1.20	n.d.	n.d.
P_2O_5	0.40 (08)	n.a.	n.a.	n.a.	n.a.	n.a.	n.a.
Total	98.52	98.89	98.78	98.45	99.09	99.66	100.29

Typical 2 standard deviation uncertainties for the element analyzed based on counting statistics for the glass analyses are: SiO_2, 0.38; TiO_2, 0.15; Al_2O_3, 0.52; MgO, 0.20; CaO, 0.17; MnO, 0.12; FeO, 0.31; Na_2O, 0.26; K_2O, 0.09; P_2O_5, 0.13. Spinifex quench zones were analyzed both as a point analysis and with 3 different sized raster scans. Numbers in brackets following the glass analysis are the two standard deviation variances in the last two significant figures of the averages. An average analysis is given for both the low-Ti and high-Ti zones of the Cpx, see text

[a] Total iron expressed as FeO

n.a., not analyzed; n.d., not detected

a single wavelength dispersive channel. Sodium was analyzed with the wavelength dispersive system; all other elements were determined using the energy dispersive analyzer. Energy and wavelength dispersive analyses were done simultaneously at a 15 keV accelerating potential and a sample current of 2.5 nA. Energy dispersive detector live time was 100 s and wavelength dispersive peak and background times were 40 and 20 s, respectively. Data were reduced using the Link ZAF procedure based on a combination of mineral and metal standards. Mineral standards analyzed during the analytical session gave compositions within analytical uncertainty of reported values.

A suite of 24 trace elements was determined on the Cameca 3f ion probe at W.H.O.I., using a 35–40 nA primary beam of O^- (20–30 μm spot size). The REE, Hf, Pb and Ba were analyzed utilizing secondary ions with an energy filtering window of +30 to +90 volts; the other trace elements were filtered with a +80 to +140 V window. Ti was analyzed with an 0.2 nA primary oxygen beam, spot size ~10–15 microns, filtered with an 80–140 eV window. Long experience on this ion probe has shown that ions with these energy levels are free of oxide and other isobaric molecular contaminants. To verify this, careful isotope ratio measurements were made for a number of elements in both Cpx and glass; in all cases, the measured ratios agreed with accepted values to within measurement precision (e.g., the four major isotopes of Zr were within 1%/amu of nominal, etc.). Europium concentrations were not attainable because of BaO interferences (Ba/Eu in the glass is ~300). Typically, small groups of elements of a given mass range were measured together (and referenced to ^{30}Si) to achieve maximum inter-element precision. All Cpx spots were checked for Ba, to insure that no glass phase was present in the analysis spot.

Table 2. Cpx-melt partitioning data, MB-41

Element	Melt concentration ppm[a]	D Cpx/melt[b]	D 2 sigma percent	Number of spots Cpx/glass
Ba	738	0.00068	27.0	6/4
K	10,375	0.0072	15.2	6/4
Nb	45.7	0.0077	10.6	6/4
B	105	(0.036)	56.0	5/2
Be	2.42	0.047	7.7	5/2
La	25.1	0.0536	6.1	6/6
Pb	–	0.072	33.4	2/2
Ce	51.5	0.0858	6.1	9/7
Sr	766	0.1283	3.7	10/4
Nd	29.1	0.1873	6.1	6/6
Zr	236	0.1234	1.3	8/4
Hf	5.99	0.256	5.0	8/6
Sm	6.72	0.291	4.6	6/6
Cu	–	0.36	10.0	2/2
Ti[c]	16,900	0.384	2.8	42/16
		(0.546	1.9	26/16)
Dy	5.94	0.442	8.4	6/6
Y	26.7	0.467	3.9	6.4
Er	3.34	0.387	3.6	8/9
Yb	3.15	0.430	4.3	8/9
Lu	0.389	0.433	5.2	6.6
Li[c]	12.0	0.59	11.3	3.2
		(0.42	3.4	2/2)
Ga	–	0.74	9.0	2/2
Sc	20.6	1.31	3.9	6/4
Cr[c]	108	3.8	8.5	3/4
		(2.7	3.7	3/4)
V[c]	170	3.1	12.0	3/4
		(4.0	5.2	3/4)

[a] Melt concentrations were determined to precisions of 5–10% only. Standards were not available for Cu, Pb and Ga. B data is suspect, see text

[b] Derived from the ratio of the ion current for a given element, relative to Si, in Cpx and glass, normalized by the observed SiO_2 abundances for Cpx and glass given in Table 1

[c] Partition coefficients for these elements refer to the low-Ti core and high-Ti rim Cpx zones respectively. The former are believed to be closest to equilibrium values

The glass was found to be very homogeneous, with element/silicon ratios constant within measurement precision (which ranged from 0.2–3.1%, averaging 1.6%). The Cpx was very homogeneous for some elements and almost bi-valued for other elements. For example, 8 different spots gave a Zr/Si dispersion of only 1.1% (2σ). In contrast, Ti/Si ratios show zoning-type variations of up to 75% (see below). Other elements which showed this bivariate nature were B, Li, V and Cr. Partition coefficients were calculated by referencing each Cpx spot to the average of all glass spots; the resulting ratios were averaged, and the precision (2σ) propagated from both the scatter of these ratios and the precision of the glass analyses. The resulting partition coefficients are listed in Table 2.

To verify that the partitioning data are not subject to contamination effects from the piston/cylinder assembly, we also list absolute trace element concentrations measured in the glass in Table 2, and plot them in a spidergram, Fig. 2. As shown by Hart and Davis (1978), open system effects can occur without leading to significant phase heterogeneity. In their case, nickel loss from the melt to the platinum container led to high olivine/melt partition coefficients, even though both olivine and melt remained homogeneous. The only real test for contamination problems is to look for aberrant element concentrations compared to the starting material. Figure 2 shows a rather smooth spidergram, as expected for an alkali basalt, with minor anomalies at K, Sr and Y. Of the other element concentrations in Table 2, Be, Li, Sc, Cr and V are all within the range typical for alkali basalts, and only B appears aberrant, being at least a factor of 10 too high. Boron also shows a very large range of concentration in the Cpx, by a factor of

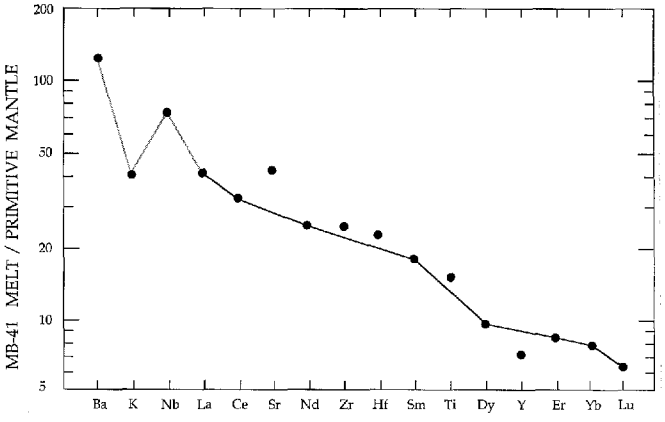

Fig. 2. Spidergram for melt fraction of MB 41 experimental charge, derived from concentrations given in Table 1 normalized to the primitive mantle concentrations of Hofmann (1988). The ordering of elements is as given by Sun and McDonough (1989), chosen largely to provide smooth spidergrams for oceanic basalts. The *solid line* connects only the REE data. The spidergram is relatively smooth, with negative anomalies for K and Y, and positive anomalies for Sr, Zr, Hf and Ti

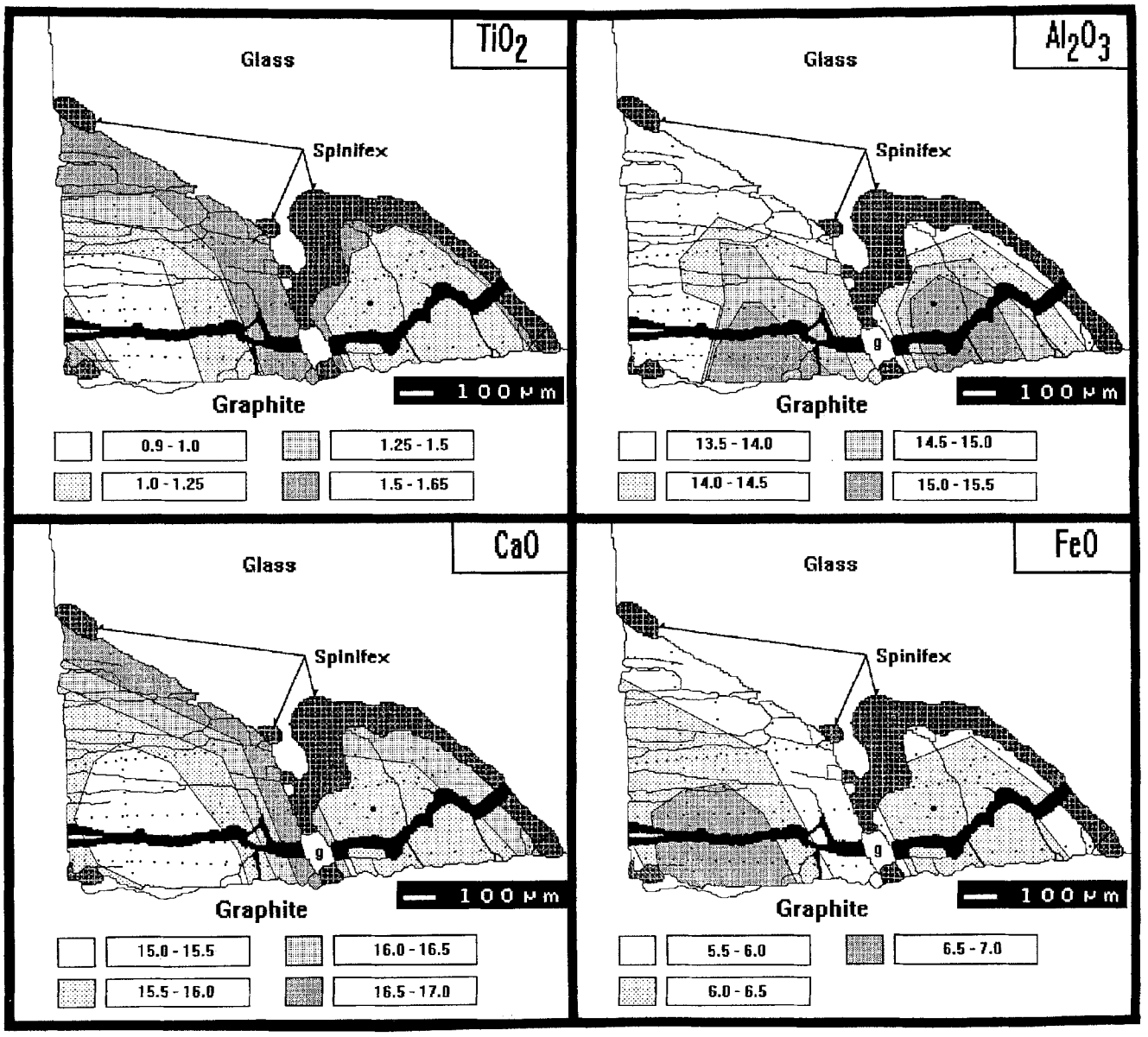

Fig. 3. Contour maps of wt% CaO, TiO_2, Al_2O_3 and total iron as FeO for the two pyroxene crystals (Fig. 1). Bold points mark electron microprobe analysis points (84 in large crystal, 33 in small crystal). Growth zoning is defined clearly by the CaO, TiO_2 and FeO concentration patterns. The Al_2O_3 distribution also shows the growth zoning pattern, but it is offset from the patterns defined by the other elements. Note that the Ti- and Ca-enriched rim is much narrower on the smaller crystal than that on the larger crystal

almost 6. We conclude that B has diffused into the charge, probably from the Pyrex sleeve, and that the partition coefficient calculated in Table 2 is far too low (B concentrations are highest toward the margins of the Cpx).

As another test of possible open system problems, we have analyzed some of the run charges of Dunn (1987). In one experiment, glass chips doped with various levels of Lu and Hf were packed next to each other in graphite powder, and run together at 1,265° C, 1.5 GPa for 67 hours. While there is clear evidence for Hf migration from a high (0.36%) Hf glass across into a Hf-free glass, separated by only 0.1–0.2 mm of graphite powder, the effect is not quantitatively large. In the present experiment, where the charge is separated from the AlSiMag by a 10 times greater thickness of solid graphite, we expect no significant elemental transport (we ascribe the B problem above to the very large concentration gradient coupled with a high diffusion rate for B).

Note that in Table 2 we have chosen to calculate partition coefficients directly from element/silicon ratios in Cpx and glass, using the SiO_2 contents given in Table 1 as normalizing factors. The implicit assumption is that the various elements sputter/ionize with the same efficiency (relative to Si) from both basalt glass and Cpx. While there is abundant evidence that this assumption is good at the 5–10% level (N. Shimizu, personal communication), standards are not currently available to demonstrate this at the 1% level. Ray and Hart (1982) reported data which showed 30% lower efficiencies (relative to Si) from glass than from Cpx, but their study utilized synthetic Fe-free glasses and a mixture of natural and synthetic Cpx. Within the rather large errors of their study (7–22%), they found no measurable differences between different trace elements (Ti, Sr, Sc, Cr). As we are most concerned with the interelement partitioning relationships (and less so with the absolute Ds), we have chosen to report to data "as is," without possible degradation by convoluting it through imperfectly known standards.

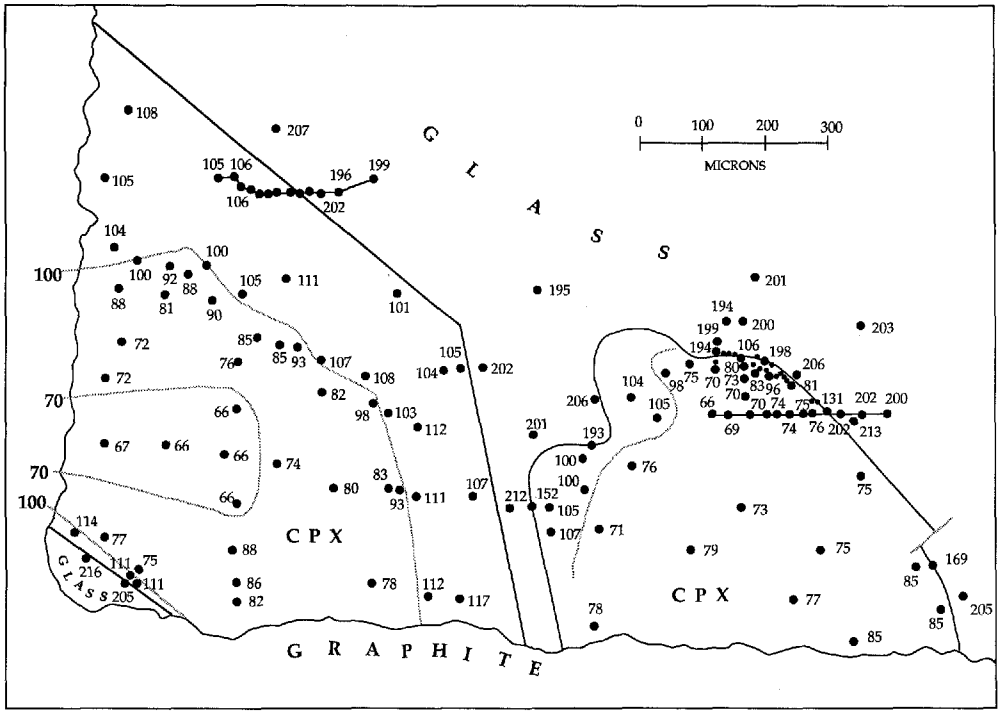

Fig. 4. Ion microprobe map of Cpx crystals in experimental charge, with values of Ti/Si shown at each analysis *spot* (numbers are mass 47 cps/mass 30 cps, times 1,000). Size of symbol is approximately the size of the analysis spot. Ti/Si contours of 70 and 100 are shown by *dashed lines*. Precision of each spot is ±1–2%. The N-NE edge of the small crystal was studied in great detail in our attempt to constrain the width of the high-Ti rim. For clarity, some points are shown small and Ti/Si values have been omitted

Equilibrium considerations

Both crystals have variable width zones of apparent quench crystals at their margins (Fig. 1a). The quench zones exhibit spinifex textures (Fig. 1b), indicative of rapid crystal growth, which suggests that these zones probably formed during quenching of the sample. Electron microprobe analyses of the apparent quench zones using different size raster scans (24×24, 12×12, and 6×6 μm) gave compositions within analytical uncertainty of crystal-free glass (Table 1). Focused beam analyses gave slightly different values. These results indicate that the quench crystallized zones retain the bulk composition of the glass at the scale of the smallest electron microprobe spots (6×6 μm); thus, these analyses of the quench zones can be taken as representative of the glass adjacent to the Cpx during crystal growth.

It is apparent that the Cpx crystals are not in internal compositional equilibrium. The major element compositions of the two pyroxene crystals have been studied in detail. One hundred and seventeen electron microprobe and 85 ion microprobe analyses were used to construct contour maps of the crystals (Figs. 3, 4). In general, the crystals appear concentrically zoned in a number of elements. Specifically, both crystals have variable width rims enriched in CaO and TiO_2 and relatively depleted in total iron expressed as FeO (FeO*) and Al_2O_3. The absolute concentrations of SiO_2, MgO and Na_2O are constant within analytical uncertainty except for narrow (<50 μm) Na_2O-depleted rims. However, due to the FeO* depletion, the rims of the crystals have higher Mg nos. than do the cores. The rims are quite distinct and relatively homogeneous, though they may be of different widths for different elements. For example, detailed ion probe traverses of the NE edge of the small crysal show that the high-Ti zone is less than 10–15 microns wide, whereas the width of the high-Ca zone is of the order of 50 microns. Also it may be noted that the Al and Ti zoning contours of the large crystal appear offset from each other (Fig. 3), suggesting a certain amount of kinetic "decoupling" of these various elements. The zoning patterns suggest growth zoning and further, that the growth occurred in two stages. Based on the widths of the rims and the similarity of the zoning patterns, the two crystals appear to represent different sections through similar crystals, rather than fundamentally different crystals. The larger crystal appears to be a section near the growth surface, while the smaller crystal is likely a section closer to the middle of the crystal.

Consideration of diffusion data for Sr and Sm in diopside reported by Sneeringer et al. (1984) clearly shows that, even at a temperature of 1,380° C and pressure of 3 GPa, diffusion scale lengths in the 22 hours of the present experiment would only be 300 microns at best. This is consistent with the Cpx/melt reversal experiment of Ray et al. (1983) which showed incomplete reequilibration even after 31 days at 1,300° C. The conclusion from such considerations might be expressed as "if a Cpx doesn't initially crystallize in equilibrium with a melt, it is very difficult to have it attain equilibrium by diffusion." While the large size of the Cpx crystals

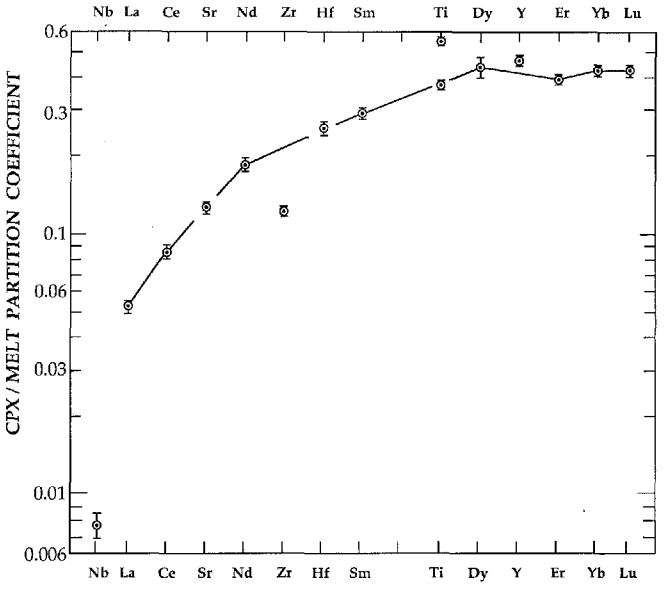

Fig. 5. Cpx/melt partitioning spidergram for sample MB 41, from data in Table 2. Error bars shown are ± 2 sigma. A number of elements are not plotted, either because their partition coefficients are very low (Ba, 0.00068; K, 0.0072) or their order in the spidergram is not well known (B, Be, Li, Cu, Ga, Sc, Cr, V). While the value for Pb has a large error due to its low concentration in the Cpx, it falls close to the REE spidergram if plotted between La and Ce. Both the high- and low-Ti values are shown. The *solid line* connects only the rare earth data; Sr, Hf and the low-Ti data plot very close to the REE curve, while Y lies slightly above it. Only Zr is clearly anomalous relative to the REE, lying almost a factor of two below the curve

in this experiment mitigates against achieving or maintaining equilibrium, their size does allow a much more detailed study of growth heterogeneity than is typical for experimental partitioning studies.

Several other elements are also distributed quasi-bimodally between the core and rim zones, with V being 29% higher in the high-Ti rim zone, and Cr and Li being 41% and 40% lower in the high-Ti rim zone relative to the low-Ti core zone. The existence of such bimodal heterogeneity is suggestive of a sector zoning effect (Kouchi et al. 1983), and the averaged growth rate of our Cpx ($\sim 5 \times 10^{-7}$ cm/s) is comparable to the rates which produced sector zoning in the Kouchi et al. (1983) study. However, the quantitative nature of the variations is not compatible with the sector zoning study of Shimizu (1981). Shimizu showed that elements such as Al, Cr, V and Ti were *all* depleted in the fast growth sector, even though Al and Ti are incompatible and Cr and V are compatible elements in Cpx; in the present study, Al, Cr and Li behave opposite to Ca, V and Ti. In addition, Shimizu (1981) showed that Zr behaved very much like Cr and V in sector zoning disequilibria; in the present study, Zr is the most homogeneous element in the Cpx. Also, Fig. 3 shows that the Cpx is not actually bimodal in composition but tends to vary continuously in composition; this is more compatible with some form of growth zoning. It is obviously not conventional fractional crystallization zoning, as the core to rim elemental variations are far too large to be caused by a crystal/melt ratio of ~ 0.1, especially considering that the elements Ca, Al, Na, V and Li are reverse-zoned (Ti and Cr are "normally" zoned, but show core to rim changes of $\sim 40\%$).

We suggest that the zoning is caused by disequilibrium partitioning *during* Cpx growth as a result of interface attachment kinetics. Alternatively, McKay et al. (1986) have argued that small, kinetically induced changes in boundary layer melt composition can amplify into large variations in Cpx composition during crystal growth. In any event, based on the Ti relationships in the crystal growth experiments of Kouchi et al. (1983) and the cooling rate experiments of Grove and Bence (1979) and Shimizu (1983), it is clear that the high-Ti rim of our Cpx is likely to be furthest from equilibrium (disequilibrium consistently increases the Ti partition coefficient). For those elements which are not homogeneously distributed in the Cpx, we argue that the *core* values will be nearest to equilibrium. Both sets of values have been reported in Table 2 and, for Ti, plotted in Fig. 5.

Discussion

We will not attempt a comprehensive review of how our data compares with previous Cpx/melt partitioning data. Suffice it to say that our REE data is about in the middle of the published range (see Frey et al. 1978 and Irving 1978). While our data show a somewhat steeper pattern than most other experimental data, they are comparable in this respect to the results of McKay et al. (1986). Our Cr, Sc and V data are within the range of values reported by Lindstrom (1976), Schreiber (1976) and Dunn (1988), though our Sc value is lower than the range reported by Gallahan and Nielsen (1992). Our Ba, K and Sr values are similar to those reported by Shimizu (1974) and Hart and Brooks (1974). Our Pb value is much higher than the value of 0.01 reported by Watson et al. (1987), and is more in line with that expected based on an incompatibility comparable to Ce (Hofmann 1988). Our Cu value is significantly lower than the range (1.5–2.4) reported by Seward (1971), and we know of no extant Cpx partitioning data for Li, Be or Ga. Based on the geochemical behavior of Be and Li in oceanic basalts, Ryan and Langmuir (1987, 1988) infer that Be is similar to Nd and Li is similar to the heavy REE, during melting processes. This information relates to bulk partition coefficients, so it is not directly comparable to Cpx partitioning. Though our Li value is indeed comparable to the heavy REE, our Be value is a factor of four lower than Nd. A bulk D^{Be} for melting could thus mimic Nd only if olivine and opx have Ds$\sim$Nd; preliminary results suggest D^{Be} in olivine and opx are ≤ 0.15 (C. Sen and T. Dunn, unpublished data). Niobium partition coefficients of 0.02 (McCallum and Charette 1978), ≤ 0.02 (Dunn and McCallum 1982), < 0.008 (Dunn 1988), 0.06 (Johnson and Kinzler 1989) and 0.005 (Green et al. 1989) have been reported; our value of 0.0077 agrees well with the Dunn, and Green et al. value,

but is significantly lower than the others. Our Y value of 0.47 is in the range reported by Kuehner et al. (1989), and Gallahan and Nielsen (1992), but lower than the value of 0.9 reported by Green et al. (1989) and higher than the range (0.16–0.27) reported by Dunn (1988).

Recently Salters and Hart (1989, 1991) have shown that the coupling of the Sm/Nd and Lu/Hf isotopic systems can provide powerful constraints on the depth of the melting zones for both OIB and MORB. This kind of modeling depends heavily on the relationship between Hf and REE partitioning characteristics of Cpx and garnet and until now there has been only one study (Fujimaki et al. 1984) which determined Hf and the REE on the same sample. Our results (Fig. 5) show that Hf plots essentially on the REE spidergram (i.e., no Hf anomaly in the spidergram), whereas Fujimaki et al. report a minor negative Hf anomaly in the case of natural phenocryst/matrix pairs, and a significant (~25%) negative Hf anomaly in the one experimental Cpx/melt run.

For the melting model of Salters and Hart (1989, 1991), the critical partitioning parameter (CPP) is: $\frac{Sm/Nd}{Lu/Hf}$, that is the relative extent of fractionation of the two parent/daughter systems. From Table 1, the CPP for our data is 0.92; this compares to 1.04 for the phenocryst/matrix data of Fujimaki et al. (1984), and 1.35 for their single experimental run. Salters and Hart (1989, 1991) used a CPP value of 1.17, which is closer to the Fujimaki et al. (1984) values than the new data we report here. Since garnet has a CPP of ~0.2, our present Cpx data look a bit more "garnet-like" than the Salters and Hart or Fujimaki et al. values. This will tend to decrease the depth of initiation of melting of the MORB and OIB data modeled by Salters and Hart (1989, 1991). However, this effect will be quite small and still in no way will allow melting to begin at the shallow depths argued for by McKenzie and O'Nions (1991).

From the point of view of spidergram "anomalies", insofar as Cpx controls the bulk partition coefficients for mantle melting of elements like Hf, Zr and the light REE, our Cpx pattern has no Hf anomaly, but a major negative Zr anomaly. This means that Hf spidergram anomalies should be rare in melts from spinel lherzolite facies mantle, but that strong fractionations of the Zr/Hf and Zr/REE can be expected. White and Patchett (1984) compiled Hf and Sm data for both oceanic and island arc basalts and showed that these elements track each other quite closely, and maintain a near-chondritic Sm/Hf ratio. In contrast, Sm/Zr and Zr/Hf ratios in oceanic basalts show considerably more scatter, perhaps indicative of variations induced by the negative Zr anomaly in the Cpx partitioning spidergram (Salters 1989). By and large, however, spidergram anomalies for Zr are not common in MORB and OIB (Sun and McDonough 1989); this suggests that the Cpx effect on Zr is modulated or offset by garnet influence, as it appears that garnet has a pronounced positive partitioning anomaly for both Zr and Hf, relative to Sm and Nd (Fujimaki et al. 1984; Green et al. 1989).

Acknowledgments. This work was supported by NSF-EAR 8708372 to SRH and NSERC OGP0001893 to TD; ion probe operations are supported by NSF-EAR 8805221 to N. Shimizu; valued technical support was provided by K. Burrhus, and N. Shimizu contributed numerous probe advisories and other discussions. We especially thank G. McKay and B. Watson for their constructive reviews.

References

Dunn T (1987) Partitioning of Hf, Lu, Ti and Mn between olivine, clinopyroxene and basaltic liquid. Contrib Mineral Petrol 96:476–484

Dunn T (1988) Partitioning of group III, IV and Vb transition metals, Sr and Lu between clinopyroxene and melts: Mg # effects. EOS 69:1512

Dunn T, McCallum IS (1982) The partitioning of Zr and Nb between diopside and melts in the system diopside-albite-anorthite. Geochim Cosmochim Acta 46:623–629

Frey FA, Green DH, Roy SD (1978) Integrated models of basalt petrogenesis: a study of quartz tholeiites to olivine melilitites from South Eastern Australia utilizing geochemical and experimental petrological data. J Petrol 19:463–513

Fujimaki H, Tatsumoto M, Aoki K (1984) Partition Coefficients of Hf, Zr, and REE between phenocrysts and groundmasses. Proc 14th Lunar Planet Sci Conf, part 2, J Geophys Res 89 Suple: B662–B672

Gallahan WE, Nielsen RL (1992) The partitioning of Sc, Y and the rare earth elements between high-Ca pyroxene and natural mafic to intermediate lavas at 1 atmosphere. Geochim Cosmochim Acta 56:2387–2404

Green DH, Ringwood AE, Ware NG, Hibberson WO, Major A, Kiss E (1971) Experimental petrology and petrogenesis of Apollo 12 basalts. Proc Second Lunar Sci Conf, pp 601–615

Green DH, Sie SH, Ryan CG, Cousens DR (1989) Proton microprobe-determined partitioning of Nb, Ta, Zr, Sr and Y between garnet, clinopyroxene and basaltic magma at high pressure and temperature. Chem Geol 74:201–216

Grove TL, Bence AE (1979) Crystallization kinetics in a multiply saturated basalt magma: an experimental study of Luna 24 ferrobasalt. Proc 10th Lunar Planet Sci Conf, pp 439–478

Hart SR, Brooks C (1974) Clinopyroxene-matrix partitioning of K, Rb, Cs, Sr and Ba. Geochim Cosmochim Acta 38:1799–1896

Hart SR, Davis KE (1978) Nickel Partitioning between olivine and silicate melt. Earth Planet Sci Lett 40:203–219

Hofmann AW (1988) Chemical differentiation of the Earth: the relationship between mantle, continental crust, and oceanic crust. Earth Planet Sci Lett 90:297–314

Irving AJ (1978) A review of experimental studies of crystal/liquid trace element partitioning. Geochim Cosmochim Acta 42:743–770

Johnson KTM, Kinzler RJ (1989) Partitioning of REE, Ti, Zr, Hf, and Nb between clinopyroxene and basaltic liquid: an ion microprobe study. EOS 70:1388

Kelemen PB, Johnson KTM, Kinzler RJ, Irving AJ (1990) High-field-strength element depletions in arc basalts due to mantle-magma interaction. Nature 345:521–524

Kouchi A, Sugawara Y, Kashima K, Sunagawa I (1983) Laboratory growth of sector zoned clinopyroxenes in the system $CaMgSi_2O_6-CaTiAl_2O_6$. Contrib Mineral Petrol 83:177–184

Kuehner SM, Laughlin JR, Grossman L, Johnson ML, Burnett DS (1989) Determination of trace element mineral/liquid partition coefficients in melilite and diopside by ion and electron microprobe techniques. Geochim Cosmochim Acta 53:3115–3130

Lindstrom DJ (1976) Experimental study of the partitioning of the transition metals between clinopyroxene and co-existing silicate liquids. PhD Thesis, Univ Oregon

Lindstrom DJ, Weill D (1978) Partitioning of trnasition metals between diopside and silicate liquids—I: nickel, cobalt, and manganese. Geochim Cosmochim Acta 42:817–832

Masuda A, Kushiro I (1970) Experimental determination of partition coefficients of ten rare earth elements and barium between clinopyroxene and liquid in the synthetic silicate system at 20 kilobar pressure. Contrib Mineral Petrol 26:1209–1264

McCallum IS, Charette MP (1978) Zr and Nb partition coefficients: implications for the genesis of mare basalts, KREEP and sea floor basalts. Geochim Cosmochim Acta 42:859–869

McKay G, Wagstaff J, Yang S-R (1986) Clinopyroxene REE distribution coefficients for shergottites: the REE content of the Shergotty melt. Geochim Cosmochim Acta 50:927–937

McKenzie D, O'Nions RK (1991) Partial melt distributions from inversion of rare earth element concentrations. J Petrol 32:1021–1091

Nagasawa H, Wakita H (1968) Partition of uranium and thorium between augite and host lavas. Geochim Cosmochim Acta 32:917–921

Nielsen RL (1985) A method for the elimination of the compositional dependence of trace element distribution coefficients. Geochim Cosmochim Acta 49:1775–1779

Onuma H, Higuchi H, Wakita H, Nagasawa H (1968) Trace element partition between two pyroxenes and the host lava. Earth Planet Sci Lett 5:47–51

Ray GL, Hart S (1982) Quantitative analysis of silicates by ion microprobe. Int J Mass Spectrom Ion Phys 44:231–255

Ray GL, Shimizu N, Hart SR (1983) An ion microprobe study of the partitioning of trace elements between clinopyroxene and liquid in the system diopside-albite-anorthite. Geochim Cosmochim Acta 47:2131–2140

Ryan JG, Langmuir CH (1987) The systematics of lithium abundances in young volcanic rocks. Geochim Cosmochim Acta 51:1727–1741

Ryan JG, Langmuir CH (1988) Beryllium systematics in young volcanic rocks: implications of ^{10}Be. Geochim Cosmochim Acta 52:237–244

Salters VJM (1989) The use of Hf-isotopes and high field strength elements to constrain magmatic processes and magma sources, PhD Thesis, MIT, Cambridge

Salters VJM, Hart SR (1989) The hafnium paradox and the role of garnet in the source of mid-ocean-ridge basalts. Nature 342:420–422

Salters VJM, Hart SR (1991) The mantle sources of ocean ridges, islands and arcs: the Hf-isotope connection. Earth Planet Sci Lett 104:365–380

Schnetzler CC, Philpotts JA (1968) Partition coefficients of rare-earth elements and barium between igeneous matrix material and rock forming mineral phenocrysts. In: Ahrens LH (ed) Origin and distribution of the lements. Pergamon, London, pp 929–938

Schreiber HD (1976) The experimental determination of redox states, properties, and distribution of chromium in synthetic silicate phases and application to basalt petrogenesis. PhD Thesis, Univ Wis

Seward TM (1971) The distribution of transition elements in the system $CaMgSi_2O_6-Na_2Si_2O_5-H_2O$ at 1,000 bars pressure. Chem Geol 7:73–95

Shimizu N (1974) An experimental study of the partitioning of K, Rb, Cs, Sr and Ba between clinopyroxene and liquid at high pressures. Geochim Cosmochim Acta 38:1789–1798

Shimizu N (1981) Trace element incorporation into growing augite phenocryst. Nature 289:575–577

Shimizu N (1983) Interface kinetics and trace element distributions between phenocrysts and magma. An: Augustithis SS (ed) The significance of trace elements in solving petrogenetic problems and controversies. Theophrastus, Athens, pp 175–195

Sneeringer M, Hart SR, Shimizu N (1984) Strontium and samarium diffusion in diopside. Geochim Cosmochim Acta 48:1589–1608

Sun S-S, McDonough WF (1989) Chemical and isotopic systematics of oceanic basalts: implications for mantle composition and processes. In: Saunders AD, Norry MJ (eds) Magmatism in the ocean basins. Geol Soc Spec Publ No 42, pp 313–345

Watson EB, Othman DB, Luck J-M, Hofmann AW (1987) Partitioning of U, Pb, Cs, Yb, Hf, Re and Os between chromian diopsidic pyroxene and haplobasaltic liquid. Chem Geol 62:191–208

White WM, Patchett J (1984) Hf—Nd—Sr isotopes and incompatible element abundances in island arcs: implications for magma origins and crust-mantle evolution. Earth Planet Sci Lett 67:167–185

Editorial responsibility: J. Patchett